energies

MDPI

Article

Composite Sliding Mode Control with Disturbance Rejection for M3C in Mining Area Wind Power

Xiaoniu Zhang [1], Mao Li [2], Xinchuan Fan [2], Qingchi Wei [3] and Xinghe Ma [4,*]

[1] Pingdingshan Tian'an Coal Mining Co., Ltd., Pingdingshan 467000, China
[2] China Pingmei Shenma Holdings Group Co., Ltd., Pingdingshan 467000, China
[3] Henan Pingmei Shenma Design Institute Co., Ltd., Pingdingshan 467000, China
[4] School of Electrical Engineering and Automation, Henan Polytechnic University, Jiaozuo 454002, China
* Correspondence: maxinghe@hpu.edu.cn

Abstract

To address the degradation of steady-state performance and the limitations of conventional control strategies for modular multilevel matrix converters (M3Cs) in mining wind power applications under complex operating conditions, such as internal multi-frequency coupling constraints and power step changes, this paper proposes a super-twisting sliding mode control strategy for the M3C based on a nonlinear disturbance observer (NDO). First, a decoupled mathematical model of the M3C is established. A nonlinear disturbance observer is then designed to provide real-time online estimation of unmodeled system dynamics and external lumped disturbances. Subsequently, a super-twisting sliding mode controller based on an integral sliding surface is constructed, and the lumped disturbance estimated by the NDO is introduced into the control law as a feedforward compensation term. Using Lyapunov theory, the finite-time reachability of the super-twisting sliding variable is established, and the exponential asymptotic stability of the current-tracking error on the sliding surface is demonstrated. Finally, the effectiveness of the proposed control strategy is verified through simulations, ablation comparisons, and experiments. The ablation results further show that the NDO mainly improves disturbance estimation and compensation as well as transient recovery, whereas the STSMC mainly reduces control chattering and improves current quality, demonstrating their complementary and synergistic effects. The results indicate that the proposed control strategy provides good steady-state performance and improves the dynamic performance and robustness of the mining wind power M3C system under power fluctuations compared with conventional control methods.

Keywords: modular multilevel matrix converter; super-twisting sliding mode control; nonlinear disturbance observer; Lyapunov function; coal mine wind power

Check for updates

Academic Editor: Krzysztof Górecki

Received: 30 July 2026
Revised: 8 October 2026
Accepted: 12 October 2026
Published: 30 October 2026

Copyright: © 2026 by the authors. Licensee MDPI, Basel, Switzerland. This article is an open access article distributed under the terms and conditions of the Creative Commons Attribution (CC BY) license.

1. Introduction

Against the background of China's "dual-carbon" goals and the low-carbon transition of industrial energy use, wind power and low-frequency/fractional-frequency transmission technologies are gradually being extended to high-power industrial applications. Reference [1] systematically reviews the current research status and development trends of fractional-frequency transmission, while Ref. [2] discusses the equipment requirements of large-scale wind power bases in mining areas from the perspective of high-power permanent-magnet generator design. Meanwhile, high-power, nonlinear, and impulsive loads in coal-mine power grids can cause significant power-quality degradation and power fluctuations, and related mitigation methods have been investigated in ref. [3]. The modular multilevel

matrix converter (M3C) can directly realize AC–AC frequency conversion and features modularity, multilevel voltage synthesis, and bidirectional power flow. It has been applied to the modeling and control of low-frequency offshore wind power transmission systems [4,5]. Therefore, the investigation of highly robust M3C control for multi-megawatt wind power collection and variable-frequency energy conversion in mining areas has clear engineering significance.

The M3C is inherently a nonlinear, strongly coupled multivariable system, with significant interactions among the input/output frequency components, arm circulating currents, and submodule energy storage [6]. Existing studies have addressed the internal coupling of M3Cs through hybrid modeling and decoupling control [5] as well as circulating-current and flatness-based control [7,8]. For fault and unbalanced operating conditions, Xiang et al. [9] applied linear active disturbance rejection control to asymmetric-fault control of M3Cs, while Cheng et al. [10] developed a bilateral Lyapunov-based nonlinear control strategy for three-phase voltage imbalance. In terms of predictive control, Cuzmar et al. proposed constrained model predictive control (MPC) and long-horizon finite-control-set MPC (FCS-MPC) for intercluster energy/current coordination and constraint handling in M3Cs [11,12]. Gong et al. [13] further developed deadbeat MPC (DB-MPC) for unbalanced grid conditions to achieve fast dynamic response, fixed switching frequency, and improved current quality. Regarding internal capacitor and energy management, Cheng et al. [14] employed dual-frequency circulating-current injection to achieve arm voltage balancing, whereas Xu et al. [15] suppressed submodule capacitor-voltage ripple through arm-energy control. These studies cover modeling and decoupling, energy balancing, predictive control, and active disturbance rejection; however, their objectives and control structures differ from the NDO-STSMC-based composite disturbance-rejection scheme for the current channels proposed in this paper.

Sliding mode control (SMC), owing to its strong robustness against parameter variations and matched disturbances, has been introduced into M3C control. Reference [16] developed a cascaded M3C control scheme based on robust backstepping sliding mode control, while Ref. [17] proposed global fast terminal sliding mode control for M3Cs in offshore wind power applications. Super-twisting sliding mode control (STSMC), on the other hand, transfers the discontinuous switching action into internal dynamics, thereby yielding a continuous actual control input and alleviating high-frequency chattering while retaining the robustness of second-order sliding mode control. Reference [2] investigated super-twisting sliding mode control, fixed-time disturbance observers, and terminal/high-order sliding mode methods in permanent-magnet synchronous motors, magnetic levitation systems, aerial robots, and linear magnetic drive systems, respectively, indicating that the theoretical and application foundations of second-order sliding mode and observer-based composite control techniques are relatively mature. Therefore, this paper does not claim the use of STSMC itself or the combination of a disturbance observer with sliding mode control, as the primary source of novelty.

Moreover, combining a disturbance observer with sliding mode control to form a composite disturbance-rejection structure of "estimation–compensation–robust feedback" has already been reported in the literature. Hou et al. combined a disturbance observer with STSMC for permanent-magnet synchronous motor (PMSM) speed regulation, where disturbance feedforward compensation was used to reduce the unknown disturbance that must be handled by the sliding mode feedback loop. Duong et al. designed a disturbance-observer-based fixed-time sliding mode controller for a three-phase three-level T-type inverter and compensated the estimated disturbance through the control input channel. Bodur and Kaplan employed a super-twisting observer and second-order sliding mode control in a Buck converter to deal with input-voltage and load variations. Luan et al.

further applied a nonlinear disturbance observer to estimate load power in the DC-bus control of an energy-storage converter and fed the estimated quantity forward to the STSMC. Therefore, the composite concept of "disturbance observer + high-order/super-twisting sliding mode control" is not first proposed in this work. For M3Cs specifically, representative advanced and disturbance-rejection control methods currently include constrained MPC and long-horizon FCS-MPC [11,12], DB-MPC [13], M3C sliding mode control [16,17], and extended-state-observer (ESO)-based FLADRC/LADRC.

Overall, existing M3C control research has covered modeling and decoupling, energy balancing, predictive control, sliding mode control, and active disturbance rejection, while the composite idea of combining a disturbance observer with high-order sliding mode control has also been explored in other power-electronic systems. Accordingly, the novelty of this work does not lie in the NDO or STSMC algorithm itself. Instead, for the dual-frequency coupled current channels of the M3C, this paper constructs a coordinated disturbance-rejection architecture consisting of lumped-disturbance modeling, explicit NDO feedforward compensation, and integral-STSMC-based residual disturbance suppression [18].

The main contributions of this paper are summarized as follows:

1. Parameter variations, grid disturbances, frequency deviations, modulation errors, and unmodeled dynamics are uniformly mapped into lumped disturbances in the dq-axis current channels, and an NDO is designed for online estimation and feedforward compensation.
2. An STSMC based on an integral sliding surface is developed to robustly suppress the residual disturbances remaining after NDO compensation. Conditions for finite-time reachability of the sliding variable and asymptotic stability of the current-tracking error are also established.
3. Under a unified M3C model and identical control constraints, five comparative cases—PI, SMC, STSMC, NDO-SMC, and NDO-STSMC—are established for ablation analysis, and the practical implementability of the proposed method is further verified using a low-voltage prototype.

2. M3C Topology and Mathematical Model

2.1. M3C Topology

Figure 1 shows the topological structure of the M3C. Its core consists of nine functionally identical bridge arms arranged in a 3 × 3 matrix configuration, directly coupling the three-phase AC grid on the input side with the three-phase AC system on the output side. Each bridge arm is formed by connectingn full-bridge submodules (Sub-module, SM) in series with a bridge arm inductor L. The SM consists of a H bridge circuit connected in parallel with a capacitor, where theH bridge circuit comprises four IGBT ($T_1 - T_4$) and their anti-parallel diodes. The full-bridge submodule structure enables bidirectional voltage output and allows for energy conversion across a wide frequency range, making it suitable for different-frequency or fractional-frequency power transmission applications scenarios such as mining grid integration.

In Figure 1, $u_x(x = \text{a,b,c})$ and $u_y(y = \text{u,v,w})$ represent the input-side and output-side voltages, respectively; i_x and i_y represent the input-side and output-side currents, respectively. u_{xy} and i_{xy} represent the bridge-arm voltages and bridge-arm currents, respectively. O and N are the neutral points on the input and output sides, respectively. The three bridge arms connected to the same phase are referred to as one sub-converter; viewed from the input side, there are three sub-converters.

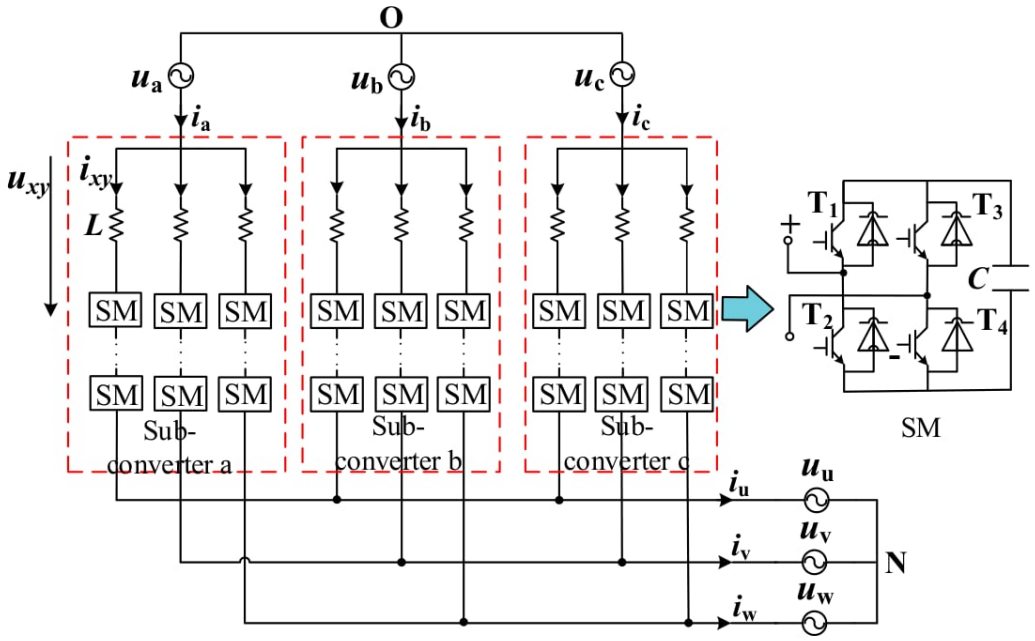


Figure 1. The main circuit topology of the M3C.

2.2. Mathematical Model

According to Figure 1, the positive direction of the arm current i_{xy}, where $x \in \{a,b,c\}$ and $y \in \{u,v,w\}$, is defined from input-side phase x to output-side phase y. To ensure consistency between the coordinate transformations and the subsequent control model, the following assumptions are adopted: The three-phase three-wire system is balanced under nominal operating conditions, with zero external zero-sequence current; the equivalent parameters of all nine arms are identical. A switching-cycle-averaged model is employed, and parameter variations, modulation errors, switching ripple, and unmodeled dynamics are uniformly incorporated into an equivalent disturbance.

First, according to the phase-domain KVL of a single arm, one obtains the following:

$$u_{sx} - u_{ry} + u_{NO} = L\frac{di_{xy}}{dt} + Ri_{xy} + u_{xy} + \Delta u_{xy} \tag{1}$$

where u_{sx} and u_{ry} denote the phase voltages of input-side phase x and output-side phase y, respectively; u_{xy} denotes the equivalent arm output voltage; u_{NO} represents the potential difference between the input-side and output-side neutral points; Δu_{xy} is the equivalent voltage disturbance; and L and R denote the arm inductance and equivalent resistance, respectively. The positive directions of the voltages and currents are defined consistently with Figure 1.

The nine arm variables are arranged into a 3 × 3 matrix, and Clarke transformations are performed along the input-side three-phase dimension and the output-side three-phase dimension, respectively. In this paper, the power-invariant orthogonal Clarke transformation matrix $T_{\alpha\beta0}$ was adopted. For an arbitrary arm-variable matrix X, the dual Clarke transformation is defined as $\tilde{X} = T_{\alpha\beta0}XT_{\alpha\beta0}^{\mathrm{T}}$.

$$\mathbf{T}_{\alpha\beta0} = \sqrt{\frac{2}{3}}\begin{bmatrix} 1 & -\frac{1}{2} & -\frac{1}{2} \\ 0 & \frac{\sqrt{3}}{2} & -\frac{\sqrt{3}}{2} \\ \frac{1}{\sqrt{2}} & \frac{1}{\sqrt{2}} & \frac{1}{\sqrt{2}} \end{bmatrix} \tag{2}$$

$$\tilde{\mathbf{X}} = \mathbf{T}_{\alpha\beta0}\mathbf{X}\mathbf{T}_{\alpha\beta0}^{\mathrm{T}} \tag{3}$$

Under three-phase balanced conditions, the external zero-sequence current is zero. According to the current scaling relationship after the dual Clarke transformation, the input-side and output-side current components satisfy the following relations:

$$\begin{bmatrix} i_{s\alpha} \\ i_{s\beta} \end{bmatrix} = \sqrt{3}\begin{bmatrix} i_{\alpha 0} \\ i_{\beta 0} \end{bmatrix}, \quad \begin{bmatrix} i_{r\alpha} \\ i_{r\beta} \end{bmatrix} = \sqrt{3}\begin{bmatrix} i_{0\alpha} \\ i_{0\beta} \end{bmatrix} \tag{4}$$

Therefore, the main current channels on the input and output sides can be separated from the dual $\alpha\beta$ model.

$$\sqrt{3}u_{s,\alpha\beta} = \frac{L}{\sqrt{3}}\dot{i}_{s,\alpha\beta} + \frac{R}{\sqrt{3}}i_{s,\alpha\beta} + u_{\alpha\beta 0} + d_{s,\alpha\beta} \tag{5}$$

$$-\sqrt{3}u_{r,\alpha\beta} = \frac{L}{\sqrt{3}}\dot{i}_{r,\alpha\beta} + \frac{R}{\sqrt{3}}i_{r,\alpha\beta} + u_{0\alpha\beta} + d_{r,\alpha\beta} \tag{6}$$

where $u_{s,\alpha\beta}$ and $u_{r,\alpha\beta}$ denote the input-side and output-side voltage vectors in the $_{\alpha\beta}$ reference frame, respectively; $u_{\alpha\beta 0}$ and $u_{0\alpha\beta}$ represent the arm voltage components obtained after the dual Clarke transformation; and $d_{s,\alpha\beta}$ and $d_{r,\alpha\beta}$ denote the corresponding lumped disturbances. The coefficients $L/\sqrt{3}$ and $R/\sqrt{3}$ in Equation (5) are directly derived from the current scaling relationships established above.

To obtain DC quantities for control, Park transformations are applied to the input-side and output-side $\alpha\beta$ components, respectively. The d-axis is defined to align with the corresponding positive-sequence voltage vector. The input-side and output-side reference angles are respectively defined as $\theta_s = \int_0^t \omega_s(\tau)d\tau$, $\theta_r = \int_0^t \omega_r(\tau)d\tau$. The Park transformation matrix and the derivative relationship in the rotating reference frame are given by the following:

$$\mathbf{T}_{dq}(\theta) = \begin{bmatrix} \cos\theta & \sin\theta \\ -\sin\theta & \cos\theta \end{bmatrix} \tag{7}$$

$$\theta_s = \int_0^t \omega_s(\tau)d\tau, \ \theta_r = \int_0^t \omega_r(\tau)d\tau \tag{8}$$

$$\mathbf{T}_{dq}\dot{\mathbf{x}}_{\alpha\beta} = \dot{\mathbf{x}}_{dq} - \omega\begin{bmatrix} 0 & 1 \\ -1 & 0 \end{bmatrix}\mathbf{x}_{dq} \tag{9}$$

By applying the Park transformation to Equation (5) and rearranging the resulting equations according to the reference-frame definitions given above, the input-side dq-axis current model used for the subsequent controller design is obtained as follows:

$$u_{d0} = \sqrt{3}u_{sd} - \frac{L}{\sqrt{3}}\dot{i}_{sd} + \frac{\omega_s L}{\sqrt{3}}i_{sq} - \frac{R}{\sqrt{3}}i_{sd} + d_{d1} \tag{10}$$

$$u_{q0} = \sqrt{3}u_{sq} - \frac{L}{\sqrt{3}}\dot{i}_{sq} - \frac{\omega_s L}{\sqrt{3}}i_{sd} - \frac{R}{\sqrt{3}}i_{sq} + d_{q1} \tag{11}$$

where u_{d0} and u_{q0} denote the arm-voltage control components in the input-side synchronous dq reference frame; u_{sd} and u_{sq} are the input-side dq-axis voltages, respectively; i_{sd} and i_{sq} are the corresponding currents; ω_s is the input-side synchronous angular frequency; and d_{d1} and d_{q1} represent the lumped disturbances in the dq-axis current channels, respectively.

According to the derivative transformation relationship in Equation (10), the cross-coupling terms in the dq-axis equations are $+\frac{\omega_s L}{\sqrt{3}}i_{sq}$ and $-\frac{\omega_s L}{\sqrt{3}}i_{sd}$, respectively. The equivalent inductive and resistive coefficients are $L/\sqrt{3}$ and $R/\sqrt{3}$, respectively, consistent with Equation (5).

Similarly, the output-side dq model can be obtained using the reference angle θ_r and angular frequency ω_r. Owing to the structural symmetry of the input-side and output-side models, only the input side is considered in the subsequent controller design.

To address the internal energy constraints, the proposed NDO-STSMC strategy is applied only to the input-side *dq*-axis current control channels. The output-side control, arm circulating current suppression, and submodule capacitor voltage balancing are implemented through independent control loops. For arm xy, the total energy stored in the submodule capacitors can be expressed as follows: $E_{xy} = \frac{1}{2}\sum_{k=1}^{N} C_{\mathrm{SM}} u_{\mathrm{C},xy,k}^2$, where C_{SM} denotes the submodule capacitance and $u_{(C,xy,k)}$ represents the capacitor voltage of the k-th submodule in the corresponding arm. The arm energy is jointly affected by the arm current, submodule insertion states, and power exchange. Therefore, input-side current control performance and internal capacitor voltage balancing are interrelated but represent two distinct verification objectives that cannot substitute for each other.

3. NDO-Based Superhelix Sliding Mode Control Strategy

Given the symmetry of the M3C topology, the design process of the control system will be detailed below using only the input side as an example.

3.1. Design of the Nonlinear Disturbance Observer

To facilitate controller design, Equations (10) and (11), which describes the input side of theM3C, is rewritten in the standard affine-nonlinear form:

$$\begin{cases} \dot{i}_{sd} = f_d + Bu_{d0} + \delta_d \\ \dot{i}_{sq} = f_q + Bu_{q0} + \delta_q \end{cases} \tag{12}$$

where

$$\begin{cases} f_d = \frac{1}{L}(3u_{sd} + \omega_1 L i_{sq}) \\ f_q = \frac{1}{L}(3u_{sq} + \omega_1 L i_{sd}) \end{cases} \tag{13}$$

$$\begin{cases} \delta_d = \frac{\sqrt{3}d_{d1}}{L} \\ \delta_q = \frac{\sqrt{3}d_{q1}}{L} \end{cases} \tag{14}$$

$$B = -\sqrt{3}/L \tag{15}$$

To estimate the unknown disturbances δ_d and δ_q, the NDO expressions for the M3C input-side *d* and *q* axes are designed as follows:

$$\begin{cases} \dot{z}_d = -k_{0_d} z_d - k_{0_d}\left(k_{0_d} i_{sd} + f_d + B\mathrm{u}_d\right) \\ \hat{\delta}_d = z_d + k_{0_d} i_{sd} \end{cases} \tag{16}$$

$$\begin{cases} \dot{z}_q = -k_{0_q} z_q - k_{0_q}\left(k_{0_q} i_{sq} + f_q + B\mathrm{u}_q\right) \\ \hat{\delta}_q = z_q + k_{0_q} i_{sq} \end{cases} \tag{17}$$

where $k_{0_d} > 0$ and $k_{0_q} > 0$ are the observer gains. z_d and z_q are auxiliary variables. $\hat{\delta}_d$ and $\hat{\delta}_q$ are the observed estimates of the lumped disturbance.

To verify the effectiveness of the designed nonlinear disturbance observer in estimating aggregate disturbances, we demonstrate this using the *d*-axis as an example.

The observation error is defined as follows:

$$\tilde{\delta}_d = \delta_d - \hat{\delta}_d \tag{18}$$

Taking the derivative of $\hat{\delta}_d$ yields, the following is obtained:

$$\begin{aligned} \dot{\tilde{\delta}}_d &= \dot{z}_d + k_{0_d}\dot{i}_{sd} = -k_{0_d}\hat{\delta}_d + k_{0_d}\delta_d \\ &= k_{0_d}(\delta_d - \hat{\delta}_d) = k_{0_d}\tilde{\delta}_d \end{aligned} \tag{19}$$

Under actual operating conditions, the external disturbance changes relatively slowly compared to the convergence rate of the observer; therefore, we can assume $\dot{\delta}_d \approx 0$.

Then, the error dynamic equation is as follows:

$$\dot{\tilde{\delta}}_d = \dot{\delta}_d - \dot{\hat{\delta}}_d = -k_{0_d}\tilde{\delta}_d \tag{20}$$

Solving Equation (20) yields the following:

$$\tilde{\delta}_d(t) = \tilde{\delta}_d(0)e^{-k_{0_d}} \tag{21}$$

As can be seen from Equation (21), the observation error $\tilde{\delta}_d$ converges to zero at an exponential rate of k_{0_d}. By increasing the observer gain k_{0_d}, the observer's tracking speed in response to disturbances can be improved, providing precise real-time disturbance feedforward compensation for the Super-Twisting Sliding Mode Control.

It should be noted that the exponential convergence conclusion in Equation (21) applies to disturbances that can be approximated as constant over continuous-time intervals. For $j \in \{d,q\}$, if the NDO estimation error satisfies

$$\delta_j = k_{(o,j)}\delta_j + \delta_j \tag{22}$$

The disturbance variation rate is bounded, i.e., $|\delta_j| \le D_j$, where $D_j \ge 0$; then, the estimation error is uniformly ultimately bounded and satisfies

$$\limsup_{t\to\infty}\left|\tilde{\delta}_j(t)\right| \le \frac{D_j}{k_{o,j}} \tag{23}$$

This indicates that increasing the observer gain helps reduce the ultimate estimation error bound under time-varying disturbances but does not guarantee that the estimation error converges exactly to zero for arbitrary time-varying disturbances. For ideal step disturbances and other discontinuous disturbances, the disturbance variation rate is bounded only within the continuous intervals between discontinuities.

3.2. Design of the Super-Twisting Sliding Mode Control

The super-twisting sliding mode algorithm is given by the following:

$$\begin{cases} u_{st} = u_{s1} + u_{s2} \\ u_{s1} = -k_1|s|^{1/2}\mathrm{sign}(s) \\ \dot{u}_{s2} = -k_2\mathrm{sign}(s) \end{cases} \tag{24}$$

$$\mathrm{sign}(s) = \begin{cases} 1, s>0 \\ 0, s=0 \\ -1, s<0 \end{cases} \tag{25}$$

where k_1 and k_2 are the gain parameters of the hyperhelix sliding mode control; $\mathrm{sign}(s)$ is a sign function; and s is the sliding surface.

The current tracking error is defined as follows:

$$\begin{cases} e_d = i_{sd}^* - i_{sd} \\ e_q = i_{sq}^* - i_{sq} \end{cases} \tag{26}$$

where i_{sd}^* and i_{sq}^* are the reference current values.

To eliminate static error, the following integral sliding surface is selected:

$$\begin{cases} s_d = e_d + c_1\int e_d \mathrm{d}t \\ s_q = e_q + c_2\int e_q \mathrm{d}t \end{cases} \tag{27}$$

where s_d and s_q are the integral sliding surfaces for the d and q axes, respectively, and c_1,$c_2(c_1 > 0, c_2 > 0)$ is the integral coefficient of the sliding surface.

Taking the derivative of Equation (27) yields the following:

$$\begin{cases} \dot{s}_d = \dot{e}_d + c_1 e_d = -\frac{3}{L} u_{sd} + \frac{\sqrt{3}}{L} u_{d0} - \omega_1 i_{sq} + c_1 e_d \\ \dot{s}_q = \dot{e}_q + c_2 e_q = -\frac{3}{L} u_{sq} + \frac{\sqrt{3}}{L} u_{q0} + \omega_1 i_{sd} + c_2 e_q \end{cases} \tag{28}$$

Setting the derivatives of s_d and s_q equal to 0, the equivalent control rate is obtained as follows:

$$\begin{cases} u_{\mathrm{eq_}d} = \sqrt{3} u_{sd} + \frac{\omega_1 L}{\sqrt{3}} i_{sq} - \frac{L c_1}{\sqrt{3}} e_d \\ u_{\mathrm{eq_}q} = \sqrt{3} u_{sq} - \frac{\omega_1 L}{\sqrt{3}} i_{sd} - \frac{L c_2}{\sqrt{3}} e_q \end{cases} \tag{29}$$

The overall control law includes the equivalent control term $u_{\mathrm{eq_}\lambda}$, the disturbance compensation term u_{obs_λ}, and the hyperhelical term u_{st_λ}, where the subscripts $\lambda = d,q$ (denote the d axis and the q axis), and is designed as follows:

$$\begin{cases} u_{d0} = u_{eq_d} + u_{obs_d} + u_{st_d} \\ u_{q0} = u_{eq_q} + u_{obs_q} + u_{st_q} \end{cases} \tag{30}$$

Using the estimates from NDO to perform real-time interference cancellation yields the following:

$$\begin{cases} -B u_{obs_d} - \hat{\delta}_d = 0 \\ -B u_{obs_q} - \hat{\delta}_q = 0 \end{cases} \tag{31}$$

From Equation (31), the perturbation compensation term for the control rate is as follows:

$$\begin{cases} u_{obs_d} = \frac{L}{\sqrt{3}} \hat{\delta}_d \\ u_{obs_q} = \frac{L}{\sqrt{3}} \hat{\delta}_q \end{cases} \tag{32}$$

Finally, the equation for the total control rate of the input-side hyperhelix sliding mode control of with respect to M3C is as follows:

$$\begin{cases} u_{d0} = \sqrt{3} u_{sd} + \frac{\omega_1 L}{\sqrt{3}} i_{sq} - \frac{L c_1}{\sqrt{3}} e_d + \frac{L}{\sqrt{3}} \hat{\delta}_d - \\ \qquad k_{1d} |s_d|^{1/2} \mathrm{sign}(s_d) - \int [k_{2d} \mathrm{sign}(s_d)] \mathrm{d}t \\ u_{q0} = \sqrt{3} u_{sq} - \frac{\omega_1 L}{\sqrt{3}} i_{sd} - \frac{L c_2}{\sqrt{3}} e_q + \frac{L}{\sqrt{3}} \hat{\delta}_q - \\ \qquad k_{1q} |s_q|^{1/2} \mathrm{sign}(s_q) - \int \left[k_{2q} \mathrm{sign}(s_q) \right] \mathrm{d}t \end{cases} \tag{33}$$

3.3. Stability Analysis

Due to the symmetry between the d axis and the q axis, this section provides a detailed stability analysis only for the d axis; the analysis for the q axis can be derived by analogy.

From Equations (12) and (28), we obtain the following:

$$\dot{s}_d = -(f_d + B u_{d0} + \delta_d) + c_1 e_d \tag{34}$$

Substituting Equation (33) into Equation (34) and simplifying yields the sliding-mode dynamic equation for the closed-loop system of the d-axis on the M3C input side:

$$\dot{s}_d = -k_{1d} |s_d|^{1/2} \mathrm{sign}(s_d) - \int [k_{2d} \mathrm{sign}(s_d)] \mathrm{d}t - \tilde{\delta}_d \tag{35}$$

For the convenience of the following analysis, Equation (35) is written in standard state-space form:

$$\begin{cases} \dot{s}_d = -k_{1d} |s_d|^{1/2} \mathrm{sign}(s_d) + \mathrm{x}_1 \\ \dot{x}_1 = -k_{2d} \mathrm{sign}(s_d) - \tilde{\delta}_d \end{cases} \tag{36}$$

Construct the Lyapunov function

$$V = \xi^T P \xi \tag{37}$$

where state vector $\xi = \left[|s_d|^{1/2} \mathrm{sign}(s_d), x_1 \right]^{\mathrm{T}}$.

P is a positive-definite matrix, designed as

$$P = \frac{1}{2}\begin{bmatrix} 4k_{2d} + {k_1}^2 & -k_1 \\ -k_1 & 2 \end{bmatrix} \tag{38}$$

Taking the derivative with respect to ξ yields

$$\dot{\xi} = \begin{bmatrix} \frac{1}{2|s_d|^{1/2}} \dot{s}_d \\ \dot{x}_1 \end{bmatrix} = \frac{A\xi}{|s_d|^{1/2}} - B\dot{\tilde{\delta}}_d \tag{39}$$

where

$$A = \begin{bmatrix} -\frac{k_{1d}}{2} & \frac{1}{2} \\ -k_{2d} & 0 \end{bmatrix}, \quad B = \begin{bmatrix} 0 \\ 1 \end{bmatrix} \tag{40}$$

Taking the derivative of the Lyapunov function V along the system's trajectory yields the following:

$$\dot{V} = \frac{1}{|s_d|^{1/2}} \xi^{\mathrm{T}} (A^{\mathrm{T}} P + PA) \xi - 2\dot{\tilde{\delta}}_d B^{\mathrm{T}} P \xi \tag{41}$$

To avoid ambiguity in the matrix notation used in the Lyapunov derivative analysis, the symmetric matrix Q is defined as $Q = -(A^{\mathrm{T}}P + PA)$. According to the matrices P and A given in Equations (33) and (35), it can be verified that when $k\{_{1d}\} > 0$. and $k\{_{2d}\} > 0$, the first leading principal minor of P satisfies $P_{11} = 2k_{2d} + \frac{k_{1d}^2}{2} > 0$ and its determinant is $\det(P) = \frac{k_{1d}^2 + 8k_{2d}}{4} > 0$. Similarly, the first leading principal minor of Q satisfies $Q_{11} = k_{1d}\left(\frac{k_{1d}^2}{2} + k_{2d}\right) > 0$, and its determinant is $\det(Q) = \frac{k_{1d}^2 k_{2d}}{2} > 0$. Therefore, both P and Q are positive definite.

Furthermore, assume that the lumped disturbance in the d-axis current channel satisfies the following condition over the continuous-time interval under consideration: $\left|\dot{\delta}_d(t)\right| \le D_d$. Combining this assumption with the estimation error dynamics derived in Section 2.1, a conservative upper bound M can be selected such that $M \ge k_{o,d}\left|\tilde{\delta}_d(0)\right| + 2D_d$,, which ensures that $\left|\dot{\tilde{\delta}}_d(t)\right| \le M$. The value of M should be conservatively determined based on the disturbance injection method, the initial state of the observer, and the simulation data rather than being arbitrarily specified. It should also be noted that the bounded-derivative assumption does not hold at the instant of an ideal step disturbance.

Based on the properties of the Lyapunov function and the Rayleigh quotient, we obtain

$$\dot{V} \le -\frac{\lambda_{\min}(Q) - 2M\left\|B^{\mathrm{T}}P\right\|_2}{\sqrt{\lambda_{\max}(p)}} V^{1/2} \tag{42}$$

where $\lambda_{\min}(Q)$ is the smallest eigenvalue of the matrix Q. $\lambda_{\max}(p)$ is the largest eigenvalue of the matrix P.

To ensure system stability, it is sufficient to design sufficiently large slip-mode gains k_{1d} and k_{2d} such that $\lambda_{\min}(Q) - 2M\left\|B^{\mathrm{T}}P\right\|_2 > 0$.

In summary, under the adopted estimation error dynamics and the assumption of piecewise bounded disturbances, if $k\{_{1d}\} > 0.$, $k\{_{2d}\} > 0$, and $\Gamma = \lambda_{\min}(Q) - 2M\left\|B^{\mathrm{T}}P\right\|_2 > 0$, then Equation (37) establishes the finite-time reachability of the sliding variable. However, the upper bound on the reaching time and the convergence properties of the tracking error should be clearly distinguished. Therefore, it is inappropriate to directly claim that the entire closed-loop system is globally finite-time stable.

The upper bound on the reaching time is given by $T_{\text{reach}} \leq \frac{2\sqrt{\lambda_{\max}(P)}\sqrt{V(0)}}{\Gamma}$. After the sliding surface is reached, if the selected integral sliding surface satisfies $s_j = e_j + c_j \int e_j dt,\ c_j > 0$, then when $s_j = 0$, the tracking error dynamics becomes $\dot{e}_j = -c_j e_j$. Consequently, the current tracking error converges exponentially to zero. However, this result does not imply that the tracking error reaches exactly zero in finite time.

The M3C control block diagram based on NDO-STSMC is shown in Figure 2.

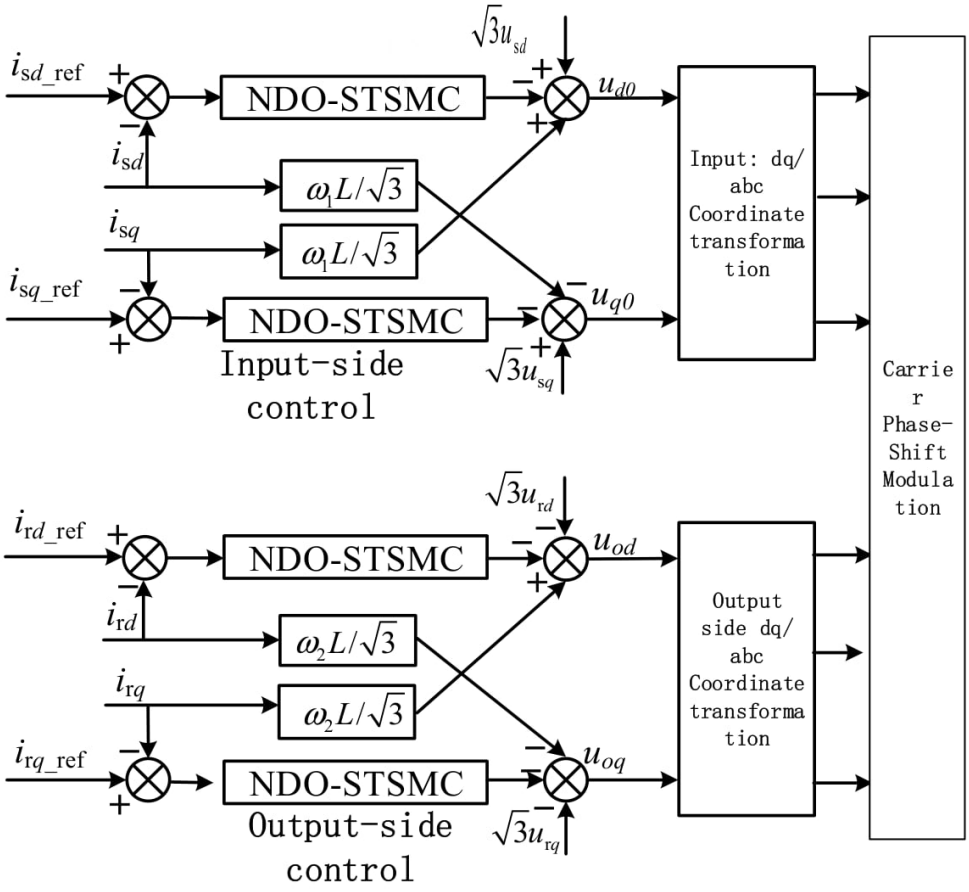


Figure 2. M3C control based on NDO-STSMC.

4. Simulation Analysis

To verify the correctness and effectiveness of the proposed M3C Super-Twisting Sliding Mode Control strategy based on a nonlinear disturbance observer, a simulation model of the M3C system for a mining area wind farm was developed on the MATLAB/Simulink R2024b software platform, and dynamic and steady-state analyses of the proposed control strategy were conducted. The main simulation parameters are shown in Table 1.

Table 1. Main parameters of the M3C.

Parameters	Values
Input line voltage/kV	10
Output line voltage/kV	10
Input frequency/Hz	50/3
Output frequency/Hz	50
Sub-module capacitance/F capacitance/F	0.02
Submodule initial voltage/kV	4.3
Number of single-girder sub-modules/pcs	3
Bridge arm inductance/mH	3

Based on the stability analysis in Section 3.1, the controller parameters were tuned; the specific parameters are shown in Table 2.

Table 2. Controller parameters.

Parameters	Values
Observer gain $k_{o\,d}$, $k_{o\,q}$	800, 800
Hyper-helical sliding-mode gain k_{1d}, k_{1q}	450, 3500
Hyper-helical sliding-mode gain k_{2q}, k_{2q}	500, 3600
Sliding-form area integral coefficient c_1, c_2	400, 420

4.1. Steady-State Analysis

Figure 3 presents the steady-state operating waveforms of the NDO-STSMC. The three-phase input and output currents remain balanced; the arm currents exhibit stable periodic envelopes, and no divergence is observed in the arm voltage. The THD of the input-side current is 1.35%, indicating that the proposed control strategy provides good steady-state current quality.

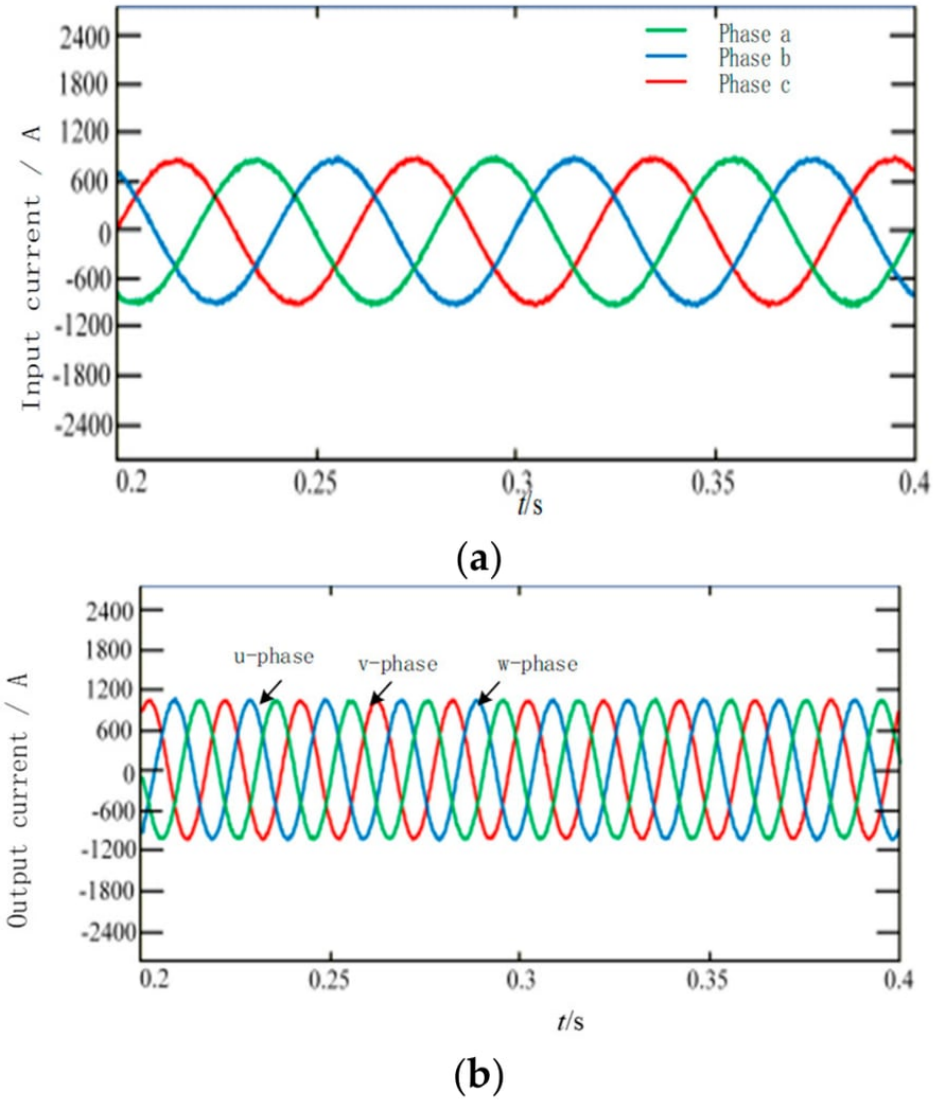


Figure 3. *Cont.*

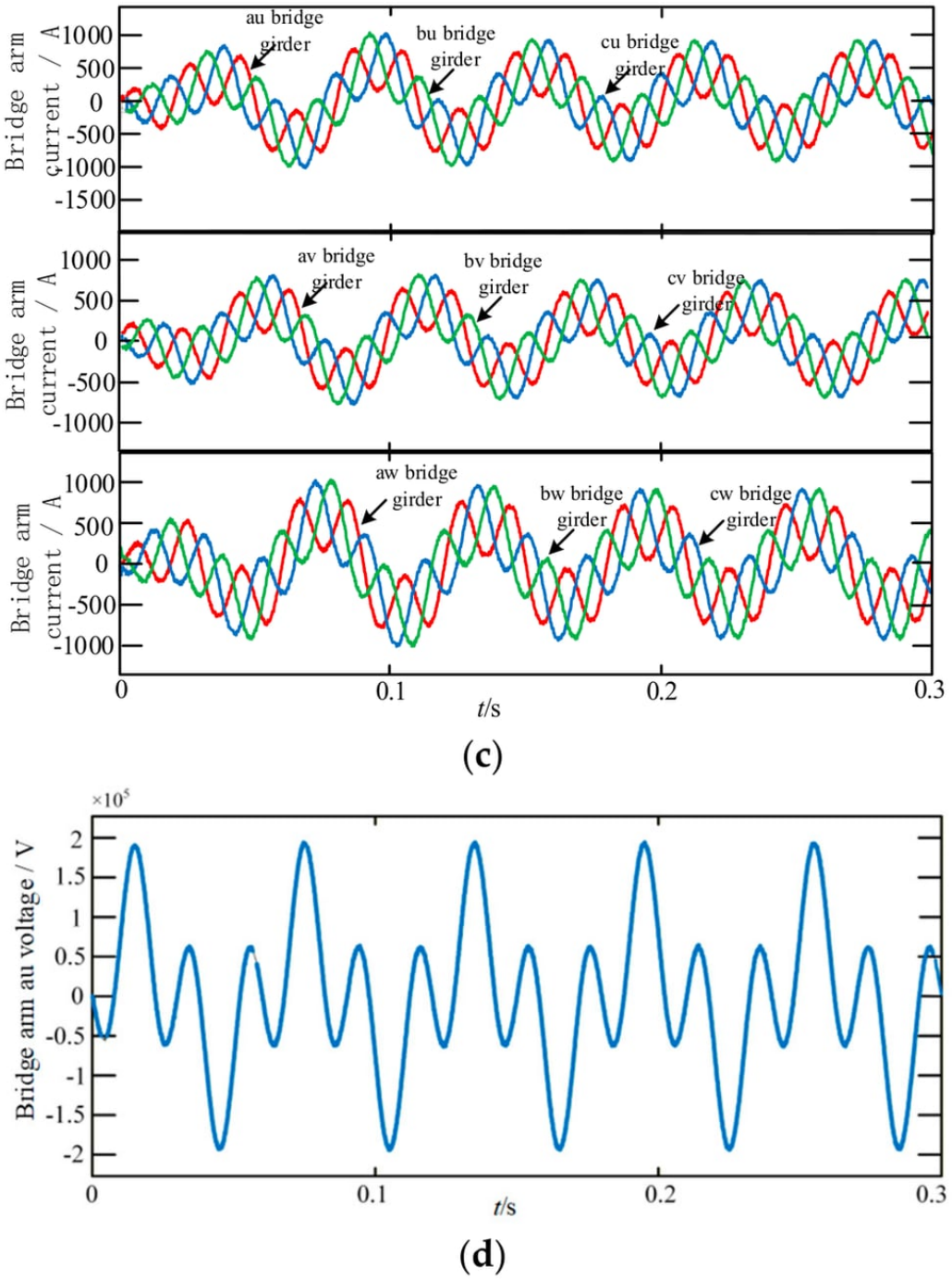


Figure 3. Simulation waveforms of the NDO-STSMC under steady-state operating conditions. (**a**) Input-side current; (**b**) output-side current; (**c**) bridge arm current; (**d**) bridge arm au voltage.

4.2. Dynamic Analysis

4.2.1. Dynamic Response to Current and Power Step Changes

Figure 4 presents the tracking responses of the d-axis current and arm current during the startup stage, demonstrating that the system can smoothly establish its operating point. The quantitative dynamic performance indices of the different controllers are subsequently evaluated in the ablation study.

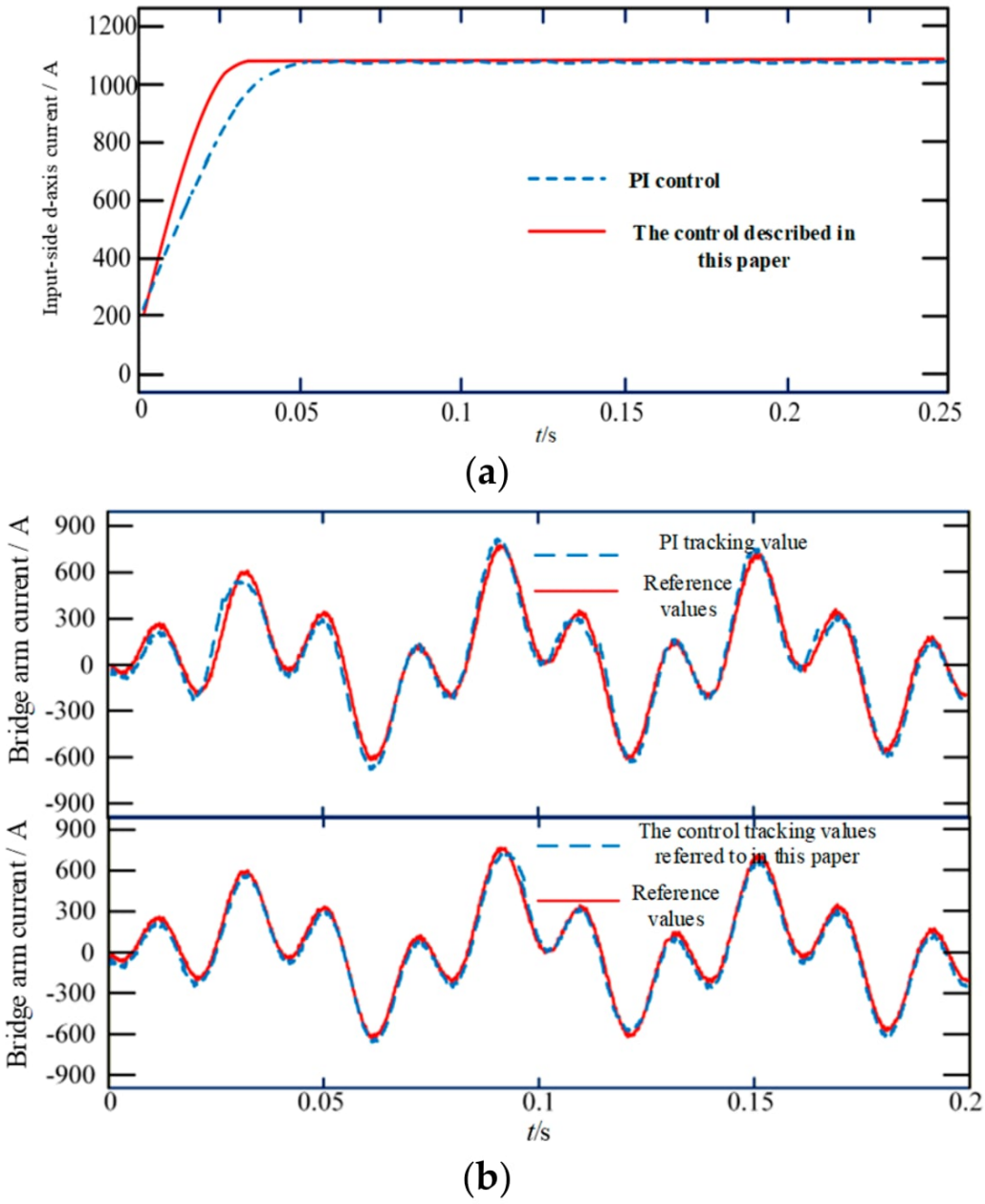


Figure 4. Waveforms under normal operating conditions. (**a**) Input-side current d-axis component; (**b**) bridge arm current tracking performance.

Figure 4b only shows the responses of the PI controller and the complete NDO-STSMC scheme, while the individual contributions of the NDO and STSMC are further distinguished through five sets of ablation comparisons.

When the system was operating in steady state at t = 0.28 s, the transmitted power was halved in a step change from 16 MW to 8 MW. As shown in the simulation results in Figure 5, under PI control, the time required for the current to reach a new steady state following a step change in power was 21 ms. In contrast, the control strategy proposed in this paper reached the new steady state in 12 ms, representing a 42.9% improvement in response speed. Comparison results indicate that the NDO-STSMC strategy enhances the robustness of the M3C system in mining area wind power projects against power fluctuations, ensuring that the system maintains excellent power conversion quality even during sudden changes in wind speed or wide-range load adjustments.

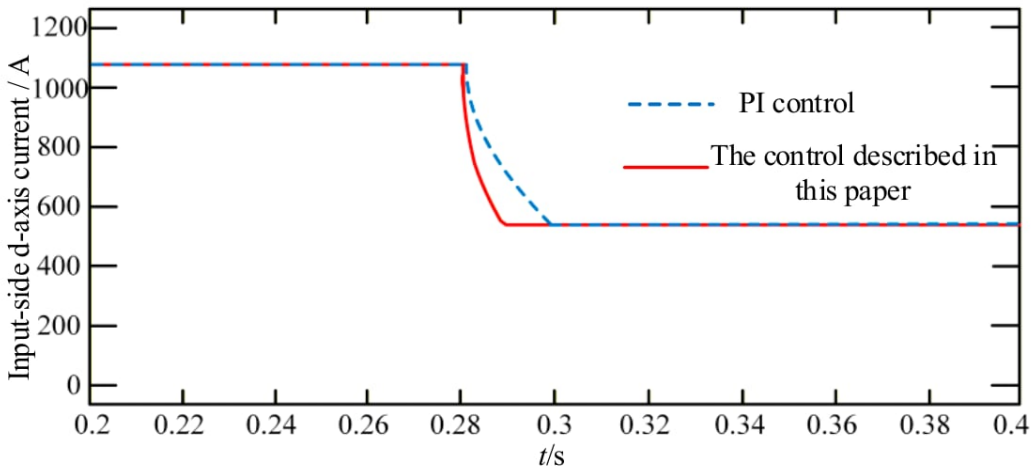


Figure 5. Input-side d-axis current under half-power conditions.

4.2.2. Ablation Analysis and Contribution Assessment of Control Components

To distinguish the roles of the individual control components, five control schemes—PI, SMC, STSMC (without NDO), NDO-SMC, and the complete NDO-STSMC—are compared under identical M3C parameters, sampling periods, initial conditions, control limits, and disturbance conditions (Table 3).

Table 3. Controller configurations for the ablation study.

Scheme	NDO	Control Structure	Purpose of Comparison
PI	No	PI	Conventional linear baseline
SMC	No	First-order SMC	Nonlinear sliding-mode baseline
STSMC	No	Integral sliding surface + STSMC	Isolate the contribution of the NDO
NDO-SMC	Yes	NDO + first-order SMC	Isolate the contribution of the STSMC
NDO-STSMC	Yes	NDO + integral sliding surface + STSMC	Complete proposed scheme

As shown in Figure 6, the PI controller exhibits relatively slow recovery under power step changes and external disturbances. The SMC improves the dynamic response but introduces pronounced high-frequency control fluctuations, whereas the STSMC significantly reduces chattering. After introducing the NDO, disturbance-estimation feedforward compensation further accelerates the recovery process. Among all the compared schemes, the complete NDO-STSMC yields the current trajectory closest to the reference value.

As summarized in Tables 4 and 5, the NDO-STSMC achieves a settling time of 32.8 ms, a maximum overshoot of 2.6%, an RMSE of 0.25 A, and a current THD of 1.35%. Compared with the PI controller, these four indices are reduced by 82.4%, 86.1%, 89.9%, and 86.8%, respectively.

Compared with the STSMC without NDO, the introduction of the NDO reduces the settling time from 56.7 ms to 32.8 ms, the RMSE from 0.72 A to 0.25 A, and the peak deviation after disturbance from 11.26 A to 3.28 A. These results indicate that the NDO mainly improves disturbance compensation and transient recovery.

Compared with the NDO-SMC, the use of STSMC reduces the maximum control chattering from 0.361 p.u. to 0.098 p.u. and decreases the THD from 2.12% to 1.35%, demonstrating that the STSMC mainly improves control continuity and current quality.

Therefore, the active disturbance compensation provided by the NDO and the robust suppression of residual disturbances achieved by the STSMC play complementary roles.

Table 4. Quantitative results of the ablation experiments (dynamic and steady-state metrics).

Method	Settling Time/ms	Maximum Overshoot/%	RMSE/A	THD/%
PI	186.3	18.7	2.48	10.24
SMC	82.6	11.2	1.18	6.46
STSMC	56.7	6.4	0.72	3.18
NDO-SMC	46.2	4.3	0.41	2.12
NDO-STSMC	32.8	2.6	0.25	1.35

Table 5. Disturbance rejection and internal-state performance metrics.

Method	Maximum Control Chattering/p.u.	Peak Deviation after Disturbance/A	Maximum Voltage Deviation/%
PI	0.312	28.45	2.63
SMC	0.876	17.38	1.72
STSMC	0.214	11.26	1.18
NDO-SMC	0.361	6.54	0.78
NDO-STSMC	0.098	3.28	0.46

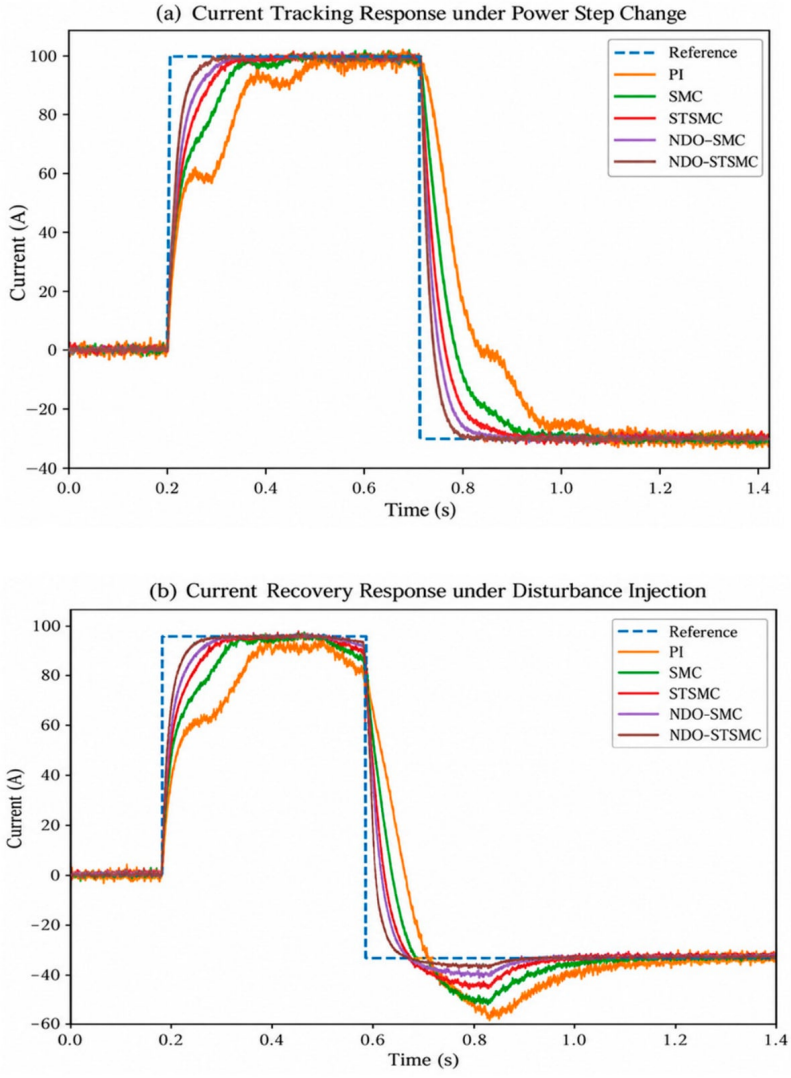
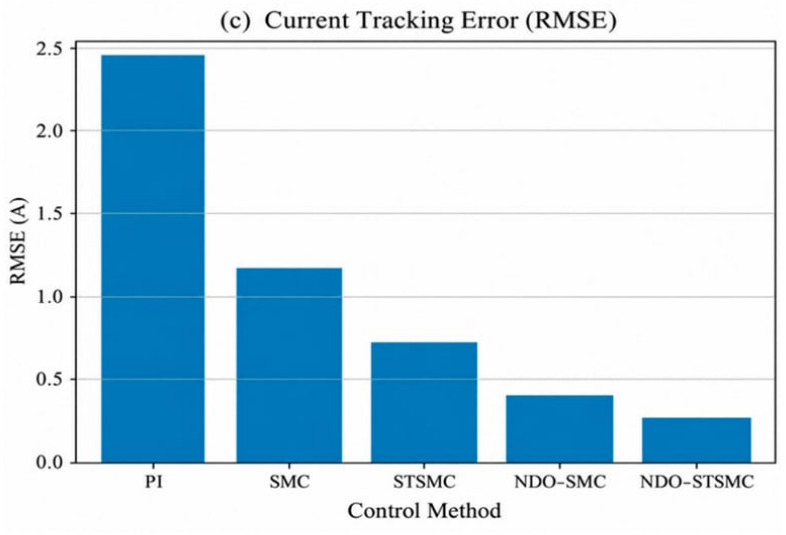
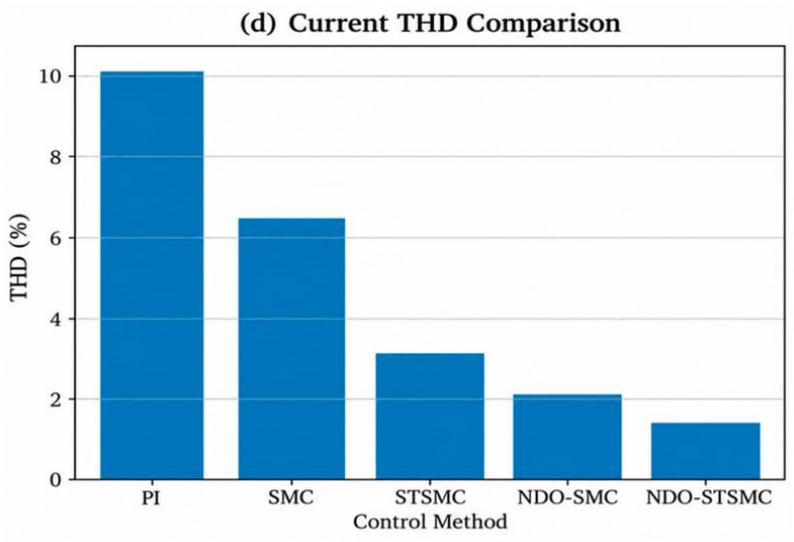


Figure 6. *Cont.*





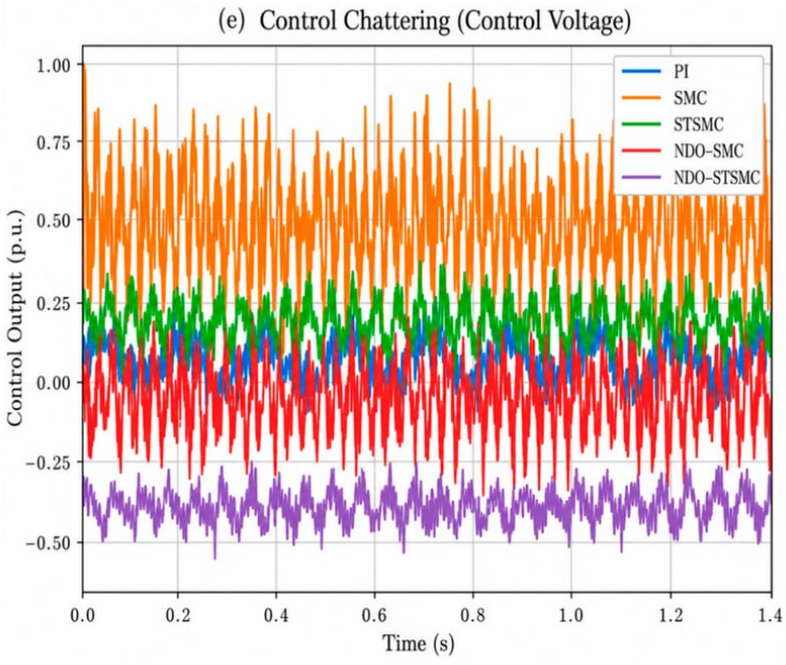


Figure 6. *Cont*.

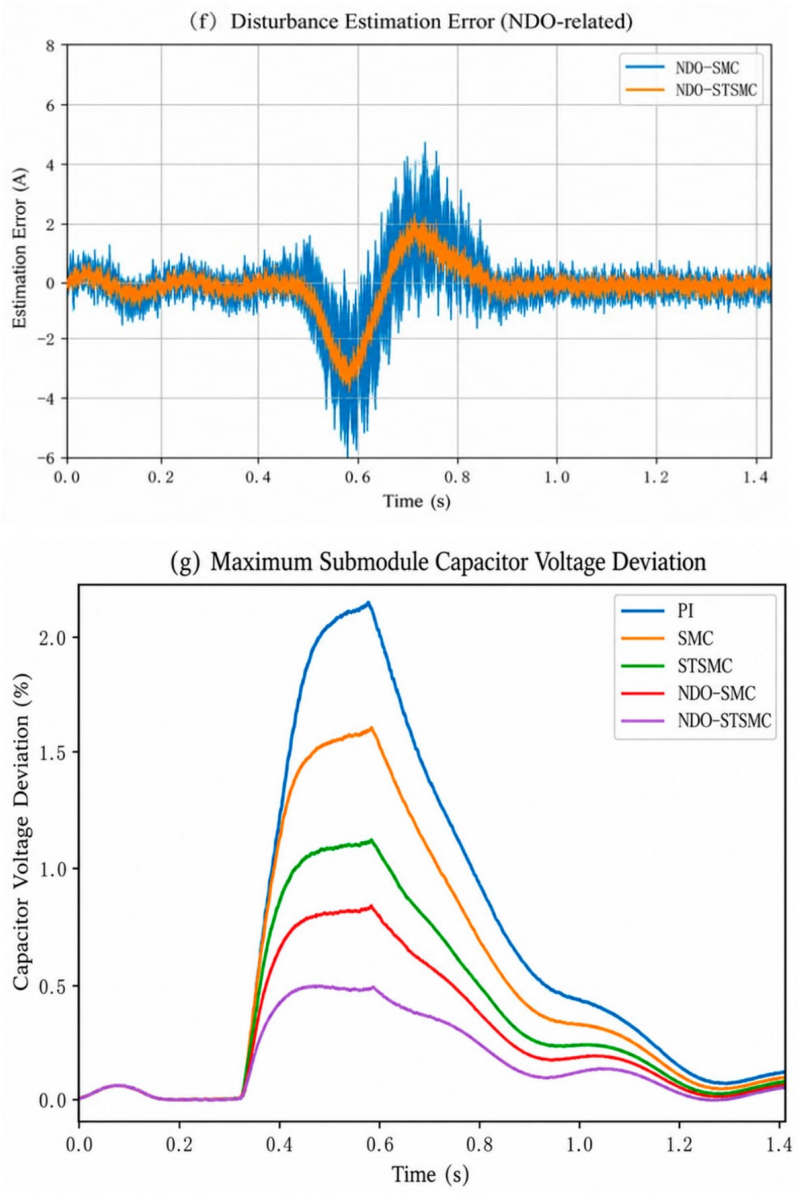


Figure 6. Ablation comparison of five control strategies: (**a**) current tracking under power step; (**b**) current recovery under disturbance injection; (**c**) current-tracking RMSE; (**d**) current THD; (**e**) control chattering; (**f**) Disturbance Estimation Error (NDO-Related); (**g**) maximum submodule-capacitor voltage deviation.

5. Experimental Analysis

To further verify the effectiveness of the proposed control strategy, experimental validation was conducted on the established experimental platform, using a DSP + FPGA controller. The experimental parameters were set as follows: input voltage of 110 V, output voltage of 110 V; input frequency of 50/3 Hz, output frequency of 50 Hz; bridge arm inductance of 0.5 mH; and submodule capacitance of 0.1 mF. Each bridge arm consists of three submodules, with each submodule rated for a voltage of 60 V. The experimental setup is shown in Figure 7.

Figure 8a,b show the experimental waveforms of the input-side current and output-side current, respectively. Both waveforms are smooth and three-phase symmetrical, with amplitudes consistent with expectations. Figure 8c shows the bridge arm currents of different sub-converters; the waveforms are of high quality and free of distortion. Figure 8d

shows the bridge arm current of sub-converter b; under the proposed control strategy, the overall envelope exhibits regular fluctuations and remains stable. To address power fluctuation conditions in mining area wind power systems caused by random wind speeds and frequent load switching, the experiment simulated an extreme scenario where the power command was halved. Figure 8e,f show the input-side and output-side currents, respectively, when the power command was halved. The results indicate that after the power change, the input-side current stabilized within 24 ms and the output-side current stabilized within 20 ms, with no overshoot or low-frequency transient oscillations observed in either case. This reveals the real-time compensatory effect of the nonlinear disturbance observer against external disturbances, thereby enhancing the dynamic robustness of the M3C system in complex grid environments.

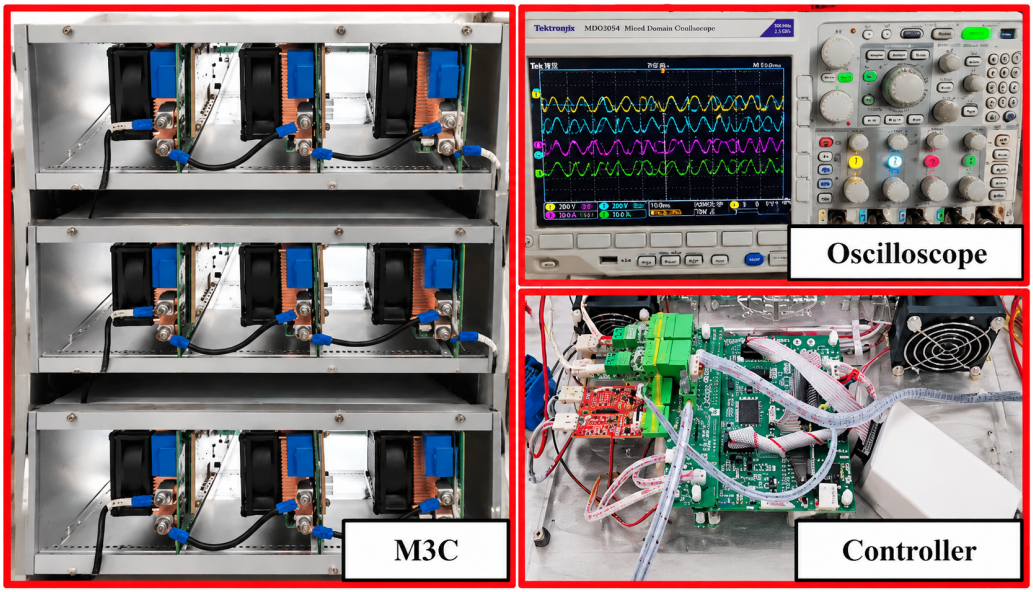


Figure 7. M3C experimental setup.

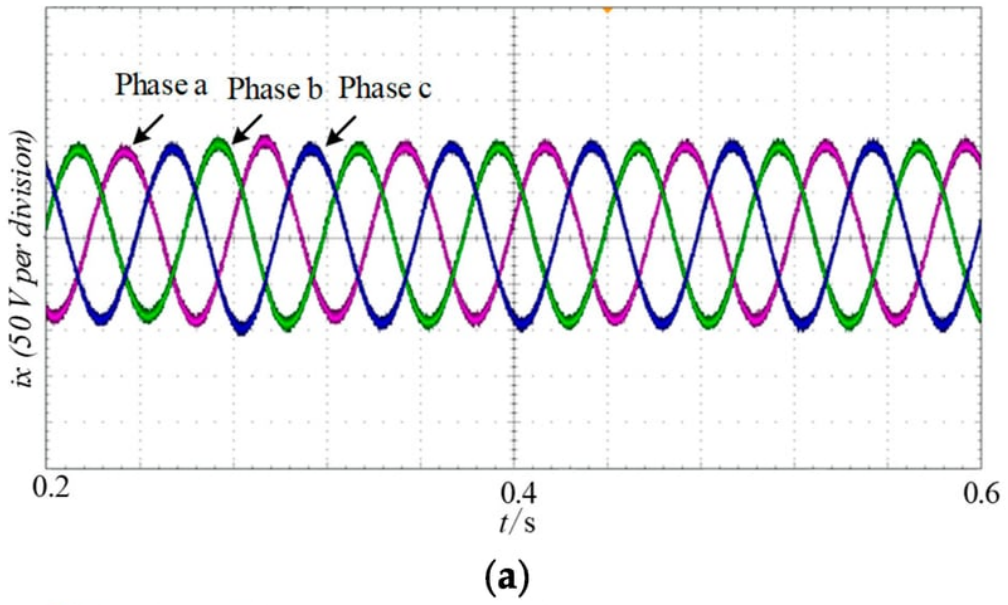
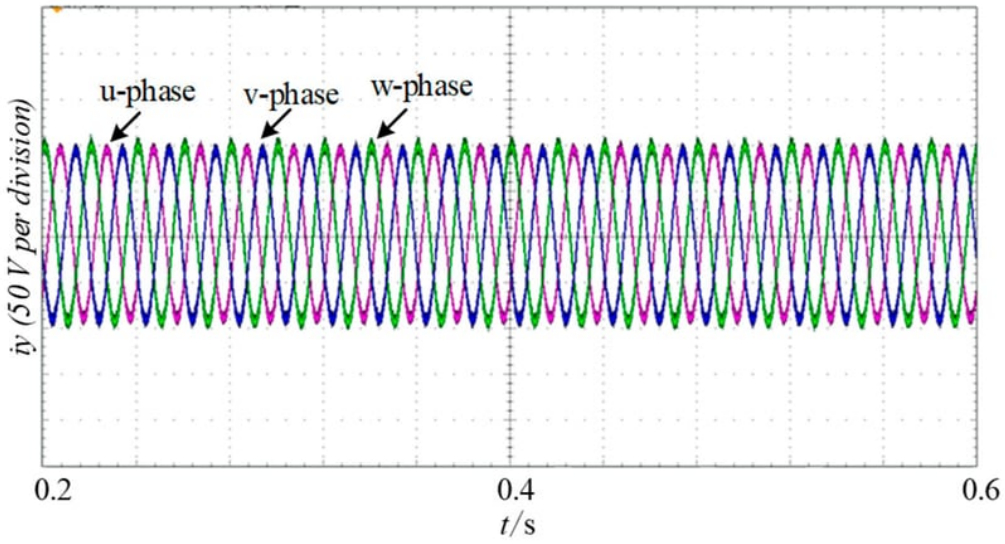
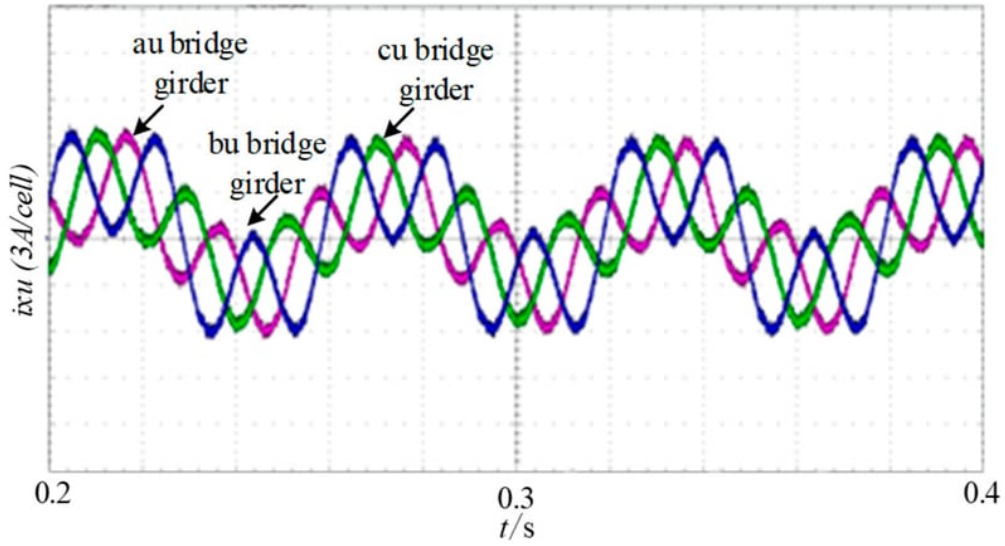


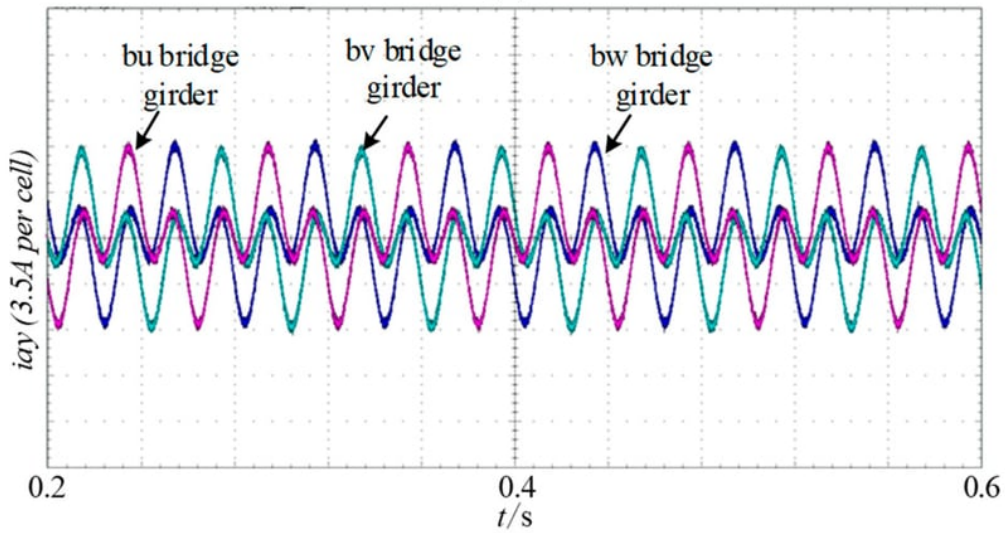
Figure 8. *Cont.*



(b)



(c)



(d)

Figure 8. *Cont.*

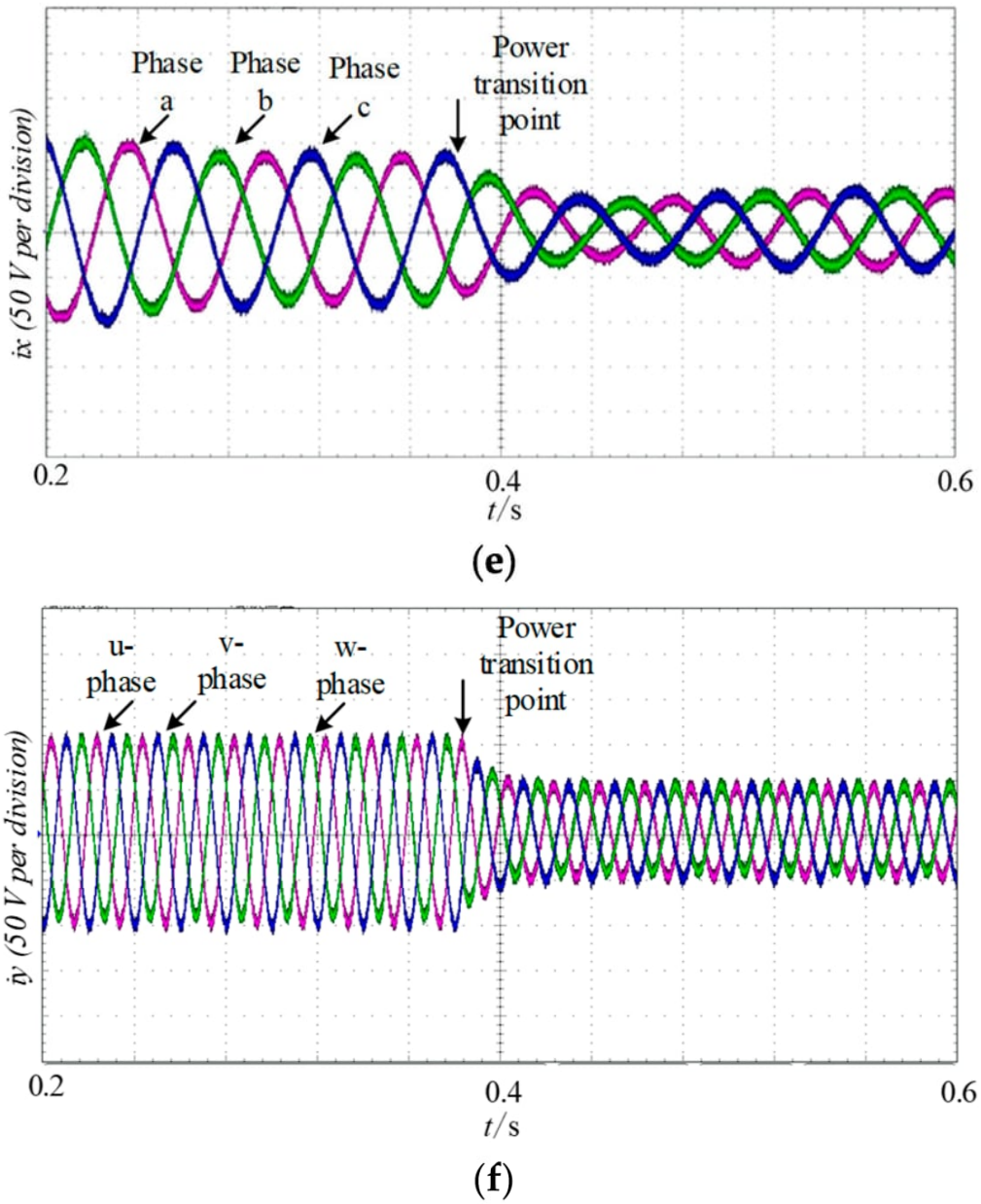


Figure 8. Experimental results waveforms. The (**a**) input current; (**b**) output current; (**c**) current in the arms of different sub-converter bridges; (**d**) current in arm B of the sub-converter; (**e**) power variation in the input current; (**f**) power variation in the output-side current.

Based on the above experimental results, the control strategy proposed in this paper not only exhibits excellent current transformation quality under steady-state conditions but also demonstrates good robustness and real-time performance during power fluctuations. The high consistency between the experimental waveforms and simulation results validates the engineering practicality of the proposed control strategy in M3C systems for wind power in mining areas.

6. Conclusions

This paper addresses the current disturbance-rejection problem of M3Cs in mining wind power applications under multi-frequency coupling and power step-change conditions. A composite control strategy combining NDO-based feedforward compensation with integral STSMC-based residual disturbance suppression is developed. Theoretical analysis demonstrates the finite-time reachability of the sliding variable and the asymptotic stability

of the tracking error, while simulation-based ablation studies and low-voltage prototype experiments verify the effectiveness and practical implementability of the proposed method. The main conclusions are as follows:

(1) The NDO can estimate the lumped disturbances in the dq-axis current channels online. When the disturbance variation rate is bounded, the estimation error is uniformly ultimately bounded; for constant or piecewise-constant disturbances, the estimation error converges exponentially.

(2) The five-group ablation study under identical operating conditions shows that the complete NDO-STSMC achieves a settling time of 32.8 ms, a maximum overshoot of 2.6%, an RMSE of 0.25 A, and a current THD of 1.35%. Compared with STSMC, the introduction of the NDO reduces the RMSE by 65.3% and the peak deviation after disturbance by 70.9%. Compared with NDO-SMC, the use of STSMC reduces the control chattering by 72.9%.

(3) The 110 V low-voltage prototype operates stably under both steady-state and half-power operating conditions, demonstrating the feasibility of digital implementation of the proposed method. Future work will further investigate multiple disturbances and engineering-parameter variations in practical mining wind power systems.

Author Contributions: Conceptualization, X.Z., M.L. and X.M.; Methodology, X.F.; Software, Q.W.; Validation, X.M.; Formal analysis, X.F.; Resources, X.Z.; Data curation, Q.W.; Writing—review and editing, X.M.; Visualization, Q.W.; Supervision, X.M.; Project administration, X.Z. and M.L.; Funding acquisition, M.L. All authors have read and agreed to the published version of the manuscript.

Funding: This research was funded by Henan Provincial Science and Technology Research Project, grant number 252102241041.

Data Availability Statement: The original contributions presented in this study are included in the article. Further inquiries can be directed to the corresponding author.

Conflicts of Interest: Author Xiaoniu Zhang was employed by the company Pingdingshan Tian'an Coal Mining Co., Ltd. Authors Mao Li and Xinchuan Fan were employed by the company China Pingmei Shenma Holdings Group Co., Ltd. Author Qingchi Wei was employed by the company Henan Pingmei Shenma Design Institute Co., Ltd. The remaining authors declare that the research was conducted in the absence of any commercial or financial relationships that could be construed as a potential conflict of interest.

References

1. Perez, M.A.; Ceballos, S.; Konstantinou, G.; Pou, J.; Aguilera, R.P. Modular multilevel converters: Recent achievements and challenges. *IEEE Open J. Ind. Electron. Soc.* **2021**, *2*, 224–239. [CrossRef]
2. Yang, Q.; Saeedifard, M.; Perez, M.A. Sliding mode control of the modular multilevel converter. *IEEE Trans. Ind. Electron.* **2018**, *66*, 887–897. [CrossRef]
3. Liu, Z.; Li, K.-J.; Guo, Z.; Wang, J.; Qian, J. A comprehensive study on the modulation ratio for modular multilevel converters. *IEEE Trans. Ind. Appl.* **2022**, *58*, 3205–3216. [CrossRef]
4. Samantaray, J.; Chakraborty, R.; Dey, A.; Chakrabarty, S. An exponential power rate discrete-time sliding mode observer for a modular multilevel converter. *IEEE Trans. Ind. Electron.* **2023**, *71*, 8227–8236. [CrossRef]
5. Xie, Z.; Zhang, Q.; Zhang, Y.; Wang, M. The linear active disturbance rejection voltage control strategy for outer-loop capacitor of M3C. In *Proceedings of the 4th Energy Conversion and Economics Annual Forum (ECE Forum 2024), Beijing, China, 14–15 December 2024*; IET: Hertfordshire, UK, 2025; pp. 721–726.
6. Wang, W.; Hang, L.; Qiu, J.; Lu, H.; Wang, S.; Chen, S. Research on control strategy of m3c matrix converter system. In *Proceedings of the 2019 22nd International Conference on Electrical Machines and Systems (ICEMS), Harbin, China, 11–14 August 2019*; IEEE: New York, NY, USA, 2019; pp. 1–5.
7. Tian, F.; Gong, J.; Zha, X.; Pan, S. A Combined M3C Suitable for Motor Drive Systems Operating at Close or Equal Input-Output Frequencies. *IEEE Trans. Power Electron.* **2026**, *41*, 9115–9132. [CrossRef]
8. Zhu, Y.; Meng, Y.; Hu, Y.; Kang, Z.; Gao, X.; Ge, M.; Zhu, D.; Zhou, Q. Harmonic analysis and suppression Strategy research of M3C converter based on fractional frequency transmission system. In *Proceedings of the 2023 26th International Conference on Electrical Machines and Systems (ICEMS), Zhuhai, China, 5–8 November 2023*; IEEE: New York, NY, USA, 2023; pp. 4263–4268.

9. Zhang, Y. Research on low frequency side short circuit fault of low frequency AC transmission (LFAC) system based on modular multilevel matrix converter (M3C). In *Proceedings of the 18th International Conference on AC and DC Power Transmission (ACDC 2022), Online, 2–3 July 2022*; The Institution of Engineering and Technology: Stevenage, UK, 2022; pp. 468–475.
10. Zhang, L.; Qin, J.; Jia, F.; Zhao, J.; Li, Z.; Zhang, Z.; Ge, X. Capacitor Voltage Self-Balancing Strategy for Modular Multilevel Matrix Converter. In *Proceedings of the 2025 IEEE International Conference on Energy Technologies for Future Grids (ETFG), Wollongong, Australia, 7–11 December 2025*; IEEE: New York, NY, USA, 2026; pp. 1–6.
11. Hou, G.; Wang, Y.; Zhang, X.; Liu, B.; Xu, Y.; Li, Y. A Novel Series-Parallel M3C Topology for Reduction of Bridge Arm Current. In *Proceedings of the 2026 6th International Conference on Advances in Electrical, Electronics and Computing Technology (EECT), Hangzhou, China, 27–29 March 2026*; IEEE: New York, NY, USA, 2026; pp. 1–6.
12. Yang, A.Z.; Gong, B.Z.; Liu, C.C.; Zhang, D.L. Wide Frequency Range Control Strategy of Modular Multilevel Matrix Converter based on FCS-MPC. In *Proceedings of the 2024 IEEE 10th International Power Electronics and Motion Control Conference (IPEMC2024-ECCE Asia), Chengdu, China, 17–20 May 2024*; IEEE: New York, NY, USA, 2024; pp. 1074–1078.
13. Liu, S.; Zhao, B.; Wang, G.; Wang, X. An improved phasor method for modelling and analysis of modular multilevel matrix converter. *IEEE Trans. Power Deliv.* **2020**, *36*, 1744–1755. [CrossRef]
14. Zhang, L.; Qin, J.; Jia, F.; Zhu, Y.; Lv, K.; Zhao, J. Sensorless control strategy for modular multilevel matrix converter. *Electr. Power Syst. Res.* **2026**, *258*, 113039. [CrossRef]
15. Zhao, B.; Li, J.; Zhang, P.; Liu, S.; Wang, X.; Wang, X. Inter-arm self-balancing characteristics of modular multilevel matrix converter. *Electr. Power Syst. Res.* **2026**, *258*, 113057. [CrossRef]
16. Cuzmar, R.; Montenegro, A.; Mora, A.; Pereda, J.; Aguilera, R.P. Constrained MPC for intercluster energy control of modular multilevel matrix converters. *IEEE Trans. Ind. Electron.* **2023**, *71*, 7766–7776. [CrossRef]
17. Yu, D.; Li, M.; Fang, J.; Jia, Z.; Hu, Z. Modular Multilevel Converters with Multilevel Submodules and Novel Capacitor Voltage Balancing Methods. *Int. J. Circuit Theory Appl.* **2026**, 1–16. [CrossRef]
18. Lin, L.; Lin, Y.; He, Z.; Chen, Y.; Hu, J.; Li, W. Improved nearest-level modulation for a modular multilevel converter with a lower submodule number. *IEEE Trans. Power Electron.* **2016**, *31*, 5369–5377. [CrossRef]

Disclaimer/Publisher's Note: The statements, opinions and data contained in all publications are solely those of the individual author(s) and contributor(s) and not of MDPI and/or the editor(s). MDPI and/or the editor(s) disclaim responsibility for any injury to people or property resulting from any ideas, methods, instructions or products referred to in the content.